Time and temperature effects on alkali chloride induced high temperature corrosion of superheaters during biomass firing

Okoro, Sunday Chukwudi; Montgomery, Melanie; Jappe Frandsen, Flemming; Pantleon, Karen

Published in:
Energy and Fuels

Link to article, DOI:
10.1021/acs.energyfuels.8b01232

Publication date:
2018

Document Version
Peer reviewed version

Process Engineering

Time and temperature effects on alkali chloride induced high temperature corrosion of superheaters during biomass firing

Sunday Chukwudi Okoro, Melanie Montgomery, Flemming Jappe Frandsen, and Karen Pantleon

Energy Fuels, **Just Accepted Manuscript** • DOI: 10.1021/acs.energyfuels.8b01232 • Publication Date (Web): 11 Jun 2018

Time and temperature effects on alkali chloride induced high temperature corrosion of superheaters during biomass firing

Sunday Chukwudi Okoro [a, b *], Melanie Montgomery [a], Flemming Jappe Frandsen [b], Karen Pantleon [a]

[a] Department of Mechanical Engineering, Technical University of Denmark (DTU), 2800 Kongens Lyngby, Denmark.

[a] CHEC Research Centre, Department of Chemical and Biochemical Engineering, Technical University of Denmark (DTU), 2800 Kongens Lyngby, Denmark.

*Corresponding author: sunoko@kt.dtu.dk, okorochukwudi@ymail.com. Phone: +45 50 18 56 80.

Abstract

The high content of alkali chloride in deposits which form during biomass firing in power plants contributes significantly to corrosion of the superheaters. In order to understand the influence of time and temperature on high temperature corrosion under such harsh conditions, laboratory scale studies as a function of time and temperature were carried out using KCl coated samples of the austenitic stainless steel (TP347H). To understand the progress of corrosion with time, isothermal exposures at 560 ^{o}C (from 83.5 h to 672 h), and at 600 ^{o}C (from 83.5 h to 168 h) were conducted in a gas mixture comprising of O_2, H_2O, CO_2, HCl and SO_2. In addition, samples were subjected to temperature variations between 560 ^{o}C and 600 ^{o}C to gain insights on the influence of temperature. The microstructure and elemental composition of the corrosion products resulting from the exposures were studied with scanning electron microscopy and energy dispersive X-ray spectroscopy, respectively. The results show that corrosion attack progressed with time such that the thickness of the consistently identified three regions of corrosion products increased with time, therefore suggesting that the corrosion products were not protective. Also, exposures under varying temperature conditions revealed

that an increased corrosion attack would always occur once the superheater experiences a higher temperature, because, a memory effect from prior exposure at higher temperature propagates more corrosion attack during subsequent exposure to a lower temperature.

Keywords: Biomass firing, Alkali chloride, High temperature corrosion, Thermal variation.

1. Introduction

The Danish energy sector aims to be powered by 100% renewable energy by 2050, and to be coal-free by 2030 [1,2]. Consequently, most coal-fired boilers are being modified for biomass use [3,4]. However, during biomass firing in power plants, corrosion of superheater tubes has been identified as a serious challenge that limits operation at high steam temperatures, thereby minimizing efficiency [3]. This challenge originates from the high content of alkali chlorides in the deposits that form on the surface of superheaters when biomass is fired in power plants [5,6]. The mechanisms behind the resulting fast corrosion of superheaters are still not completely understood due to the influence of a number of parameters such as deposit composition, temperature and flue gas chemistry. Nonetheless, Cl from the deposit has been recognized to be chiefly responsible for the fast corrosion of superheaters through the mechanism generally referred to as active oxidation [7–12].

Previous laboratory scale investigations under gaseous atmospheres mimicking biomass firing have shown that the original KCl particles in the deposit are converted to K_2SO_4 according to reaction (1) [13–16]. The resulting K_2SO_4 is less corrosive than KCl [17], and hence, technologies facilitating sulphation of KCl to K_2SO_4 in the gas phase are employed to minimize the fast corrosion of superheater tubes [18,19].

$$2KCl(s) + SO_2(g) + \frac{1}{2}O_2(g) + H_2O(g) \rightleftharpoons K_2SO_4(s) + 2HCl(g) \qquad (1)$$

However, sulphation of condensed KCl particles on the surface of the superheater tube can have serious implications for the corrosion attack, because the released HCl (see reaction 1) close to the metal surface may serve as a source of chlorine to propagate corrosion. Moreover, the present understanding of the progression of the corrosion attack with time under such conditions is inconsistent. On one hand, laboratory-scale studies with very low deposit coverage (0.01 mg/mm^2) at 600 ^{o}C [14], have revealed that conversion of KCl to the less corrosive K_2SO_4 is complete after 1 h of exposure, and accordingly,

corrosion attack should reduce significantly afterwards. However, using a high deposit coverage (0.75 mg/mm^2), laboratory-scale investigations at 560 ^{o}C [15], under the same gas atmosphere as will be employed in the present study, have shown that conversion of KCl to K_2SO_4 was below 10 % after 72 h. Consequently, the present work aims to provide an improved insight into the progression of corrosion attack with time under laboratory conditions simulating in-deposit (heterogeneous) sulphation of KCl to K_2SO_4 for durations up to 672 h.

From full scale investigations in biomass fired power plants, it has been observed that slight temperature increases above the typical steam temperature of 540 ^{o}C (which approximately corresponds to a surface metal temperature of 560 ºC) result in significantly increased corrosion rates [3]. However, as the steam temperature in actual superheaters can vary a lot due to fluctuating operating conditions, studies under controlled conditions are important to obtain proper understanding of the influence of temperature on corrosion of superheaters during biomass firing. From isothermal laboratory studies with KCl coated AISI 304 austenitic stainless steel in an oxidizing atmosphere (5% O_2 + 40% H_2O), at temperatures between 400-600 ^{o}C [20], it has been suggested that the temperature dependence of the reaction between deposits and the initial oxide on superheater surfaces (i.e. reaction 2), as well as the ability of the ensuing oxide to offer protection, govern the alkali chloride induced corrosion under different temperature conditions.

$$(\mathrm{Cr}_x\mathrm{Fe}_{1-x})_2\mathrm{O}_3(\mathrm{s}) + 4x\mathrm{KCl}(\mathrm{s}) + 1.5x\mathrm{O}_2(\mathrm{s}) + 2x\mathrm{H}_2\mathrm{O}(\mathrm{g}) \rightleftharpoons (1-x)\mathrm{Fe}_2\mathrm{O}_3(\mathrm{s}) + 2x\mathrm{K}_2\mathrm{CrO}_4(\mathrm{s}) + 4x\mathrm{HCl}(\mathrm{g}) \quad (2)$$

However, recent studies [21,22] have suggested that the corrosion process during biomass firing can involve other mechanisms such as sulphation and chlorination, thus, the influence of temperature on the corrosion mechanism may not only be limited to its effect on reaction 2. Accordingly, the present paper, by means of dedicated corrosion exposures under well-defined conditions mimicking biomass

firing, also aims to provide insights into the effect of temperature on superheater corrosion. In addition to isothermal exposures at different temperatures, the influence of thermal variations on corrosion was also investigated, with the example of variations between 560 ^{o}C and 600 ^{o}C. The temperature variations have been applied by switching from low to high temperature as well as vice versa, from high to low temperature, under otherwise the same exposure conditions that mimicked biomass firing.

2. Experimental

2.1 Sample preparation and high temperature corrosion exposures

The austenitic stainless steel TP 347H FG (fine grained, with ASTM grain size: 8.8-9.2 [23]), being a typical superheater material in thermal power plants, was used for the investigations. The chemical composition of the steel has been determined to be: 18.1 wt% Cr, 10.3 wt% Ni, 2.0 wt% Mn, 0.5 wt% Nb, 0.4 wt% Si and Fe as balance. The C-content of the steel amounts to 0.057 wt% [24]. The investigated samples were cut from the as received tube to give segments with a width of 10 mm, height of 7.4 mm with the corresponding arc length of the concave side being 14.6 mm. The samples were cleaned ultrasonically using acetone and then dried with ethanol. Afterwards, they were coated on the concave side with a deposit slurry that was obtained by mixing KCl and 2-propanol. After evaporation of the solvent, a deposit thickness of about 1mm, which corresponds to a deposit coverage of about 1 mg/mm^2, was obtained on the surface of the samples.

The deposit coated samples were exposed in a corrosion test rig that comprised of a gas mixing panel, a furnace and a gas cleaning unit. A detailed description of this setup is given elsewhere [25]. The corrosion exposures were carried out under a gas atmosphere comprising of 60 ppmv SO_2, 400 ppmv HCl, 6 vol% O_2, 12 vol% CO_2 and 82 vol % N_2 (on dry basis). This corresponds to the gas composition measured during straw firing in a power plant, with the concentration of HCl representing a worst case

scenario [13]. With the exception of SO_2 and HCl, the gas mixture was bubbled through a water bath to incorporate 3 vol% of H_2O.

Corrosion exposures were conducted under the time and temperature conditions summarized in Table 1. Experiments T1-T6 were carried out isothermally with the intention to understand the progression of corrosion with time, while experiments T7 and T8 involved thermal variations to reveal the influence of the temperature sequence, as illustrated in Figure 1. After each experiment, samples were cooled inside the furnace under a flow of the gas mixture.

Table 1. Summary of the experimental conditions investigated. All investigations involved exposure of KCl-coated TP 347H FG samples to the oxidizing-chlorinating-sulphidizing gas atmosphere.

Experiment	Temperature (^{o}C)	Time (h)
T1	560	83.5
T2		168
T3		336
T4		672
T5	600	83.5
T6		168
T7	560 → 600	168 (83.5+83.5)
T8	600 → 560	168 (83.5+83.5)

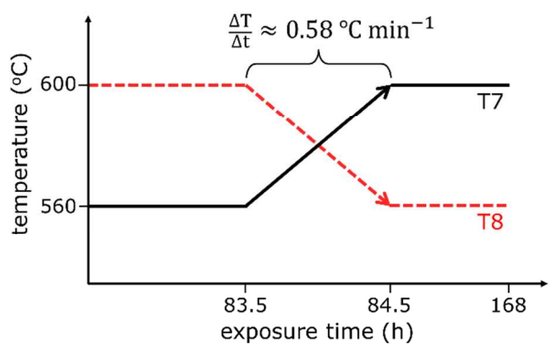

Figure 1. Schematic illustration of the thermal variation sequence in experiments T7 and T8.

2.2 Characterization of corrosion products

The corrosion products resulting from the various high temperature exposures in Table 1 were characterized by investigating cross sections of the exposed samples using Scanning Electron Microscopy (SEM) and Energy Dispersive X-ray Spectroscopy (EDS). The sample cross sections were accessed following a two-stage mounting process to preserve the corrosion products according to a previously described procedure [25]. Absolute ethanol (VWR Chemicals, 99.9 %) was utilised as lubricant during metallographic preparation due to the solubility of some corrosion products in water.

An Inspect S (FEI) was utilized for SEM characterization of the corrosion products. The microscope was operated with an acceleration voltage of 15 keV and imaging was carried out with a backscatter electron detector. EDS analysis was carried out using an Oxford silicon drift detector attached to the SEM, and was also conducted with an acceleration voltage of 15 keV.

3. Results and discussion

3.1 The influence of time

Figure 2 shows the typical morphology of corrosion products observed after isothermal exposures at 560 ^{o}C for different durations ranging from 83.5 h (Figure 2a) to 672 h (Figure 2d). As shown in a previous study [25], the morphology and composition of the corrosion products under the investigated conditions can be inhomogeneous, hence, Figure 2e schematically illustrates the representative morphology of the non-compact layers of corrosion products which generally appeared as three regions. The topmost region of corrosion products is designated as region 1 and from the observed contrast in Figure 2, it is probable that the region consists of two phases. Region 2, which contains several voids and porosities, is located below region 1, and is often separated from region 3 by a crack.

Infiltration of these cracks with the embedding epoxy suggests that they originate from sample handling, prior to or during the mounting process.

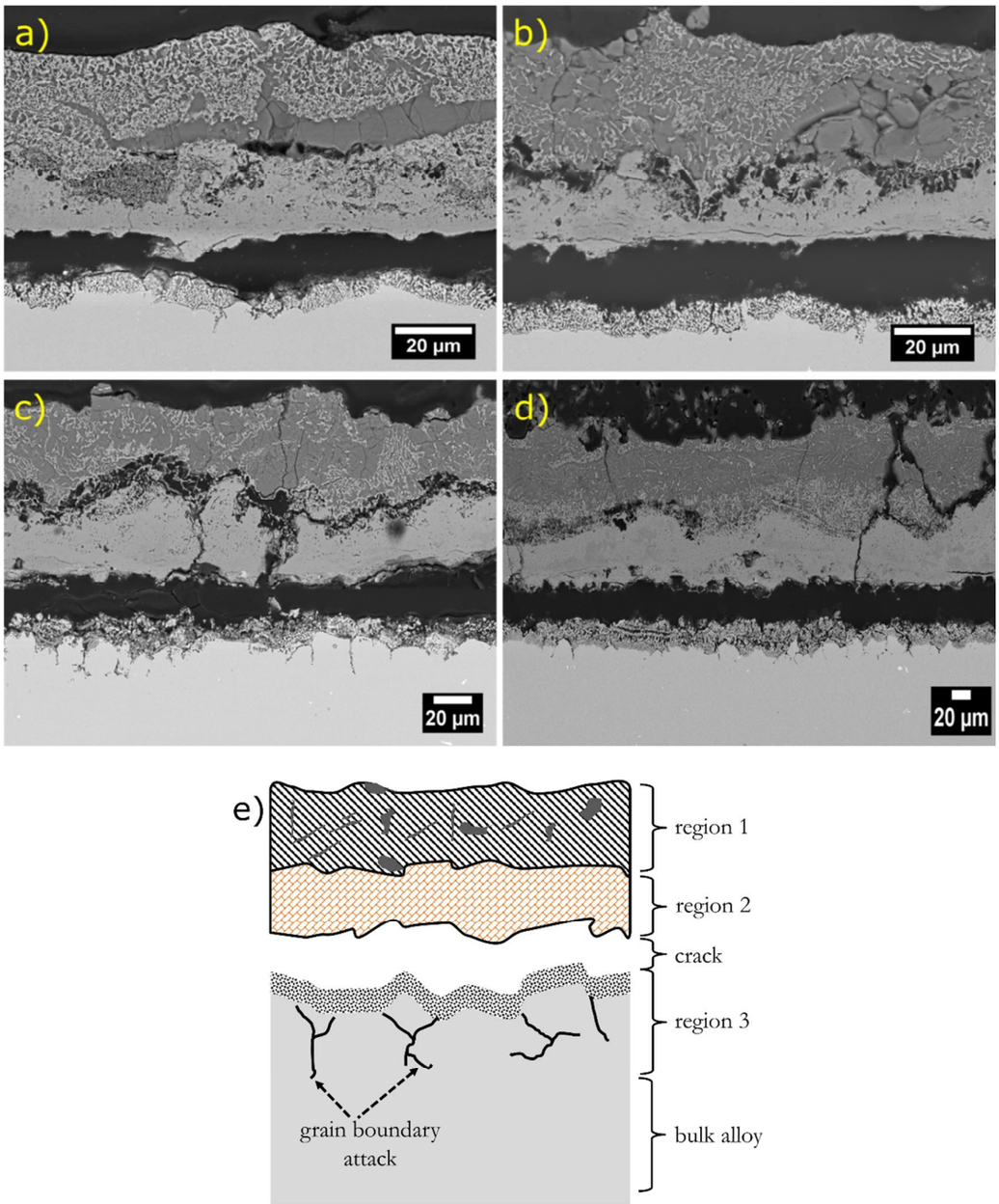

Figure 2. Morphology of corrosion products after isothermal exposure at 560 °C for different durations. (a) 83.3 h, experiment T1, (b) 168 h, experiment T2, (c) 336 h, experiment T3, and (d) 672 h, experiment T4. The schematic in (e) provides a representation of the typical regions of corrosion products.

Region 3 was typically the most porous region of the corrosion products and also includes the areas of grain boundary attack. In addition to the obvious crack between regions 2 and 3, various cracks are observed within the corrosion products and they may have originated from sample handling or preparation. As observed from the micrographs in Figure 2, the existence of the three regions of corrosion products was not altered as a function of time, rather their thicknesses varied (Figure 3).

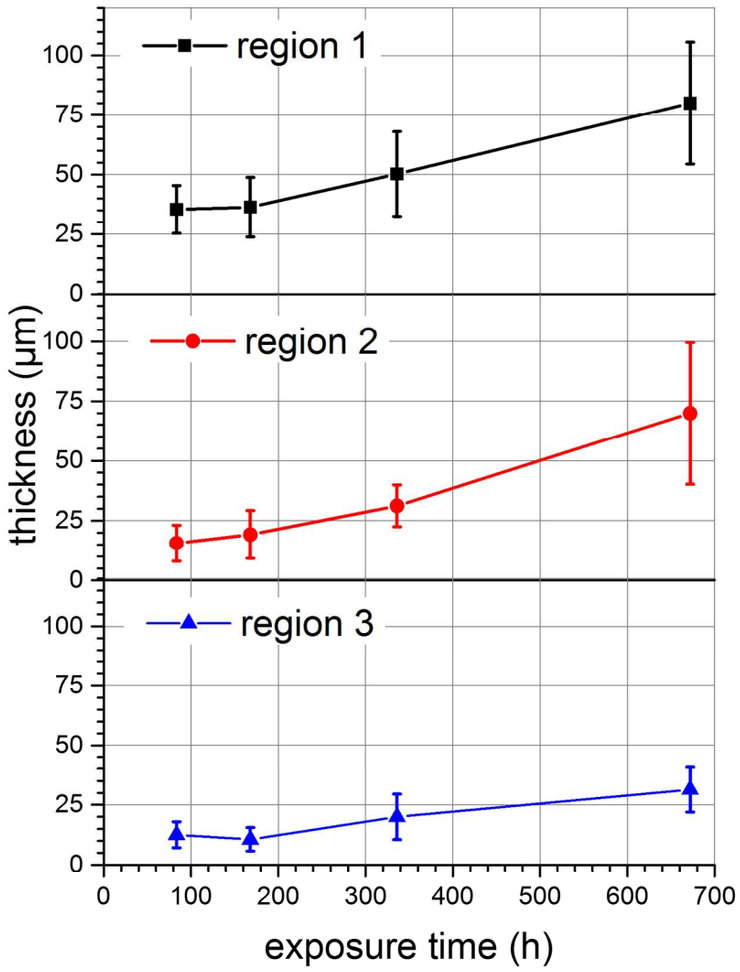

Figure 3. The mean thicknesses of the different regions of corrosion products as a function of exposure time at 560 ^{o}C (experiments T1-T4). The error bars outline the corresponding standard deviation.

The plots in Figure 3 showing the thickness of the different regions, were obtained from over 50 measurements using the commercial software ImageJ. Since the investigated alloy was the same in all

the experiments, the observed variation in thickness of the regions of the corrosion products is utilized to assess the degree of corrosion attack. The plots clearly show that the average thicknesses of the three regions of corrosion product increased with time while the large standard deviations, in particular after prolonged exposure time, reflect the non-uniform thickness of the different regions as observed in Figure 2.

Figure 4 shows the representative elemental distribution of the three regions of corrosion products on the example of a sample that was isothermally exposed at 560 ^{o}C for 672 h (cf. Fig. 2d). As observed from the elemental maps, region 1 is enriched in K, S, Mn, Fe and O with the darker features being particularly rich in K and S. Region 2 is Fe, Cr, and O rich with significant Cr enrichment in the lower parts. In region 3, strong enrichment of Ni is evident. In addition, enrichment of Cl is observed here, however, it is important to note that signals from the epoxy resin penetrating into this porous region, may have contributed to this. The composition of regions 1 and 2 are moderately consistent for the varying morphologies of corrosion products observed on different samples. However, in region 3, the composition (both within a given sample, and among different samples) occasionally deviates from being exclusively Ni-rich to include S, O and other alloying elements such as Fe or Cr. As such variation was observed even on samples isothermally exposed for 672 h, the earlier suggestion that establishment of a Ni-rich porous layer at the corrosion front is time dependent [25] cannot be confirmed in the present work.

The composition of the corrosion products and their distribution in the different regions are a consequence of the Cl-propagated mechanism of corrosion under biomass firing conditions in which chloride species in the gas or from reaction 1 induce chlorination of alloying elements at the corrosion front [8,11,15]. The tendency of Cl to selectively chlorinate Mn, Fe and Cr in austenitic stainless steels results in the observed enrichment of Ni at the corrosion front (Figure 4) and is due to the relatively low driving force for the chlorination of Ni compared to the other alloying elements [26–29]. Further, the

metal chlorides of these metals are more volatile, and in addition, relatively easier to be converted to oxides, than the metal chloride of Ni within the temperatures investigated in this work. Consequently, Fe-Cr-Mn rich oxides are identified in region 2 due to conversion of chlorides of these elements to their oxides. These oxides exhibited a porous morphology probably because the transport of the precursor metal chlorides occurred through the gas phase. As is shown by the presence of K and S in region 1 of the corrosion products (Figure 4), KCl deposited on the surface of the samples, reacts with SO_2 in the gas mixture resulting in formation of K_2SO_4 (i.e., in-deposit sulphation in accordance with reaction 1). Although the exact degree of KCl conversion to K_2SO_4 cannot be precisely followed with the characterization techniques applied in the present study, the observed increase in thickness of region 1 (Figure 3) indicates that the sulphation process (i.e., reaction 1) is still ongoing even after 672 h.

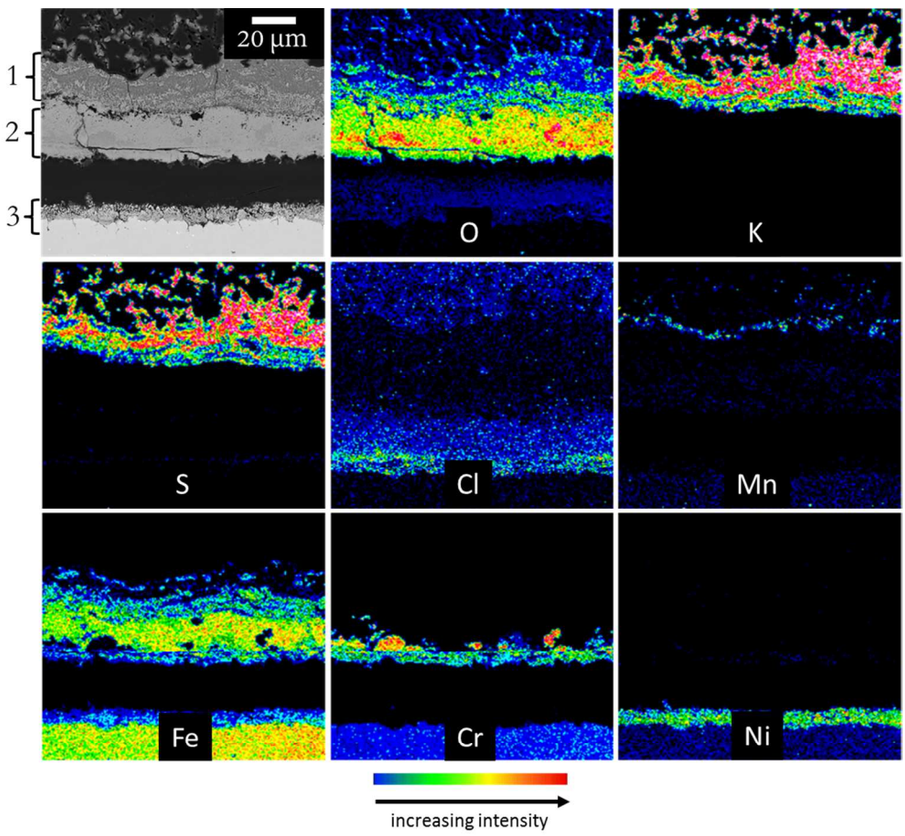

Figure 4. EDS maps showing the chemical composition of the different regions of corrosion products after 672 h of isothermal exposure at 560 °C.

Moreover, the corresponding increase in thicknesses of regions 2 and 3 suggests that the sulphate layer in region 1 does not effectively hinder the transport of corrosive species to and from the corrosion front, thereby essentially suggesting that, as long as the sulphation of the deposit is incomplete, the Cl-propagated corrosion mechanism will progress with time under a static (non-replenished) deposit, as applied in the present study. However, this Cl propagation mechanism, and partial sulphation of the deposit is very dependent on the flue gas composition. In the same set-up employed in this study, when there was no HCl in the flue gas, a totally different morphology was observed, where in some areas, there were pits and in other areas, thin 'protective' corrosion products of oxide and sulphides [30]. Increasing the SO_2 content, as was the case in simulated oxyfuel conditions with an NaCl deposit [31] also resulted in much less corrosion attack. Thus, if there is enough SO_2, a more protective sulphide can form at the corrosion front and decrease attack. How protective this is in field exposure where there is a continuous influx of new KCl deposit is difficult to assess.

Because of the non-compact nature of the corrosion products (Figure 2), it is very likely that corrosion attack under the investigated condition does not occur by solid-state diffusion, but probably, by gas phase transport of species through the porous corrosion products. This is supported by the steady increase in thickness of the different regions of the corrosion products with respect to time (Figure 3), as opposed to parabolic kinetics which should ensue assuming solid-state diffusion was the limiting mode of transport during the corrosion process, where either the deposit layer or the oxide is protective [32,33].

The influence of time on the corrosion process was also investigated at 600 ^{o}C. In Figure 5, the typical morphology of corrosion products observed after corrosion exposures at 600 ^{o}C for 83.5 h (Figure 5a) and 168 h (Figure 5b) is shown. As was observed for isothermal exposures at 560 ^{o}C (cf. Figure 2), the corrosion products after exposures at 600 ^{o}C can also be generally categorized into three regions, with

the typical local variations in region 3, both within a sample and across different samples. The typical enrichment of Ni in region 3 also occurred during corrosion exposures at 600 °C but in addition, attack along grain boundaries was pronounced (Figure 5a-c). From Figure 6, it is observed that similar to the corrosion attack at 560 °C (cf. Figure 3), the extent of corrosion at 600 °C increases with time. However, contrary to the observation at 560 °C, a clear increase in the mean thickness of the different regions is observed after 83.5 h, indicating that temperature significantly influences the corrosion mechanism. This is further addressed in section 3.2.

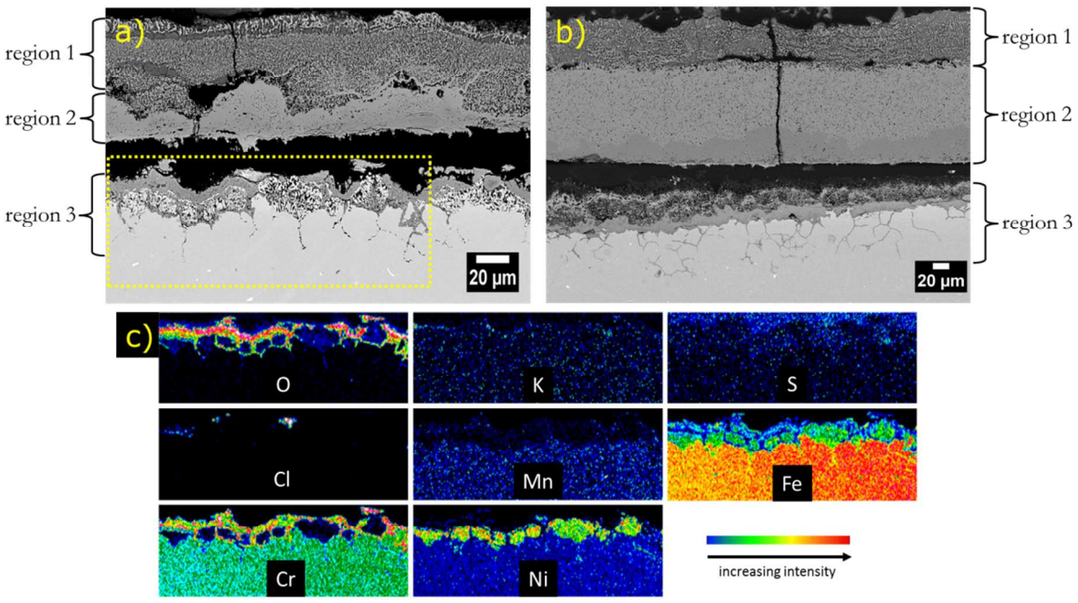

Figure 5. Morphology of corrosion products after isothermal exposures at 600 °C for (a) 83.5 h, experiment T5 and (b) 168 h, experiment T6. (c) EDS maps of the selected area in (a).

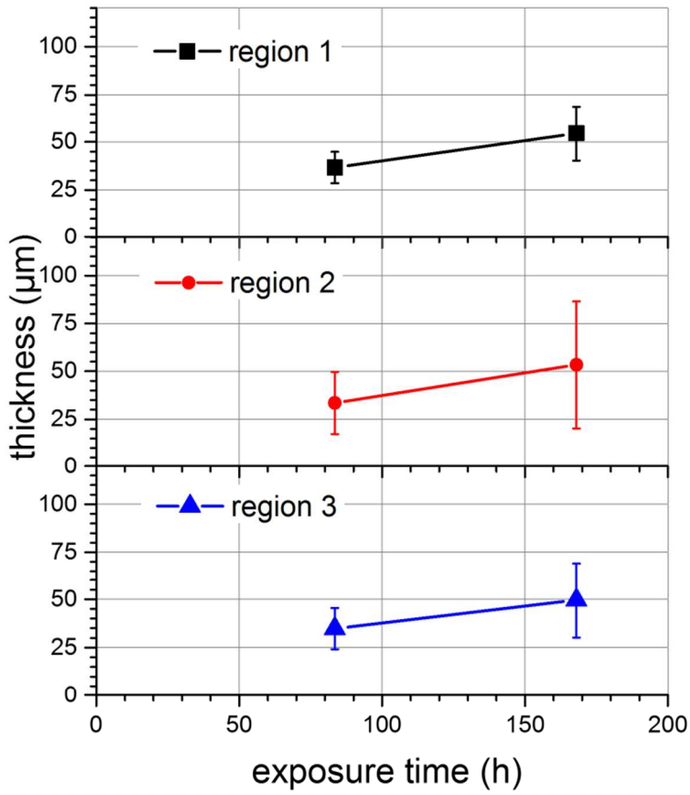

Figure 6. The mean thicknesses of the different regions of corrosion products after isothermal exposure at 600 °C for different times (experiments T5 and T6). The error bars outline the corresponding standard deviation.

3.2 The influence of temperature

By comparing Figures 3 and 6, the degree of corrosion attack during isothermal exposure at 600 °C is observed to be higher than at 560 °C after exposure to otherwise same conditions (i.e. deposit, gas atmosphere and time). Interestingly, it is also observed that after 168 h at 600 °C, the resulting thickness of region 3 (which provides an indication of the internal attack on the sample [21]), surpasses that developed after 672 h at 560 °C. The pronounced depth of grain boundary attack in Figure 5 is also in agreement with this.

To obtain more insights on how temperature influences corrosion, exposures involving thermal variations between 560 °C and 600 °C were conducted (experiments T7 and T8). The morphology of corrosion products originating from thermal variation from a low to high temperature (experiment T7),

and vice versa (experiment T8) is shown in Figure 7. Similar to isothermal exposures (Figures 2 and 5), the corrosion products resulting from exposure to conditions involving thermal variations, also consisted of three regions (Figure 7a and b), with local variation in morphology and elemental composition of the third region. However, the order of temperature variation is observed to influence the predominant morphology of corrosion products, particularly that of regions 2 and 3. The morphology of regions 2 and 3 after thermal cycling from 600 ^{o}C to 560 ^{o}C (experiment T8, Figure 7b) are similar to those observed after isothermal exposures at 600 ^{o}C (experiment T6, Figure 5b). Despite the difference in morphology, results from EDS mapping (not shown here) disclosed that the composition of the three regions of corrosion products were, in generic terms, similar to those observed after isothermal exposures. Thus, in both thermal variation scenarios, region 1 was K, S, Mn, Fe and O rich; region 2 was Fe, Cr, and O rich; while region 3 was enriched in Ni, in addition to Fe, Cr, S and O. This indicates that the order of temperature change during thermal variation only influences the degree of corrosion, and not necessarily the previously described Cl-propagated mechanism which is considered responsible for the corrosion attack.

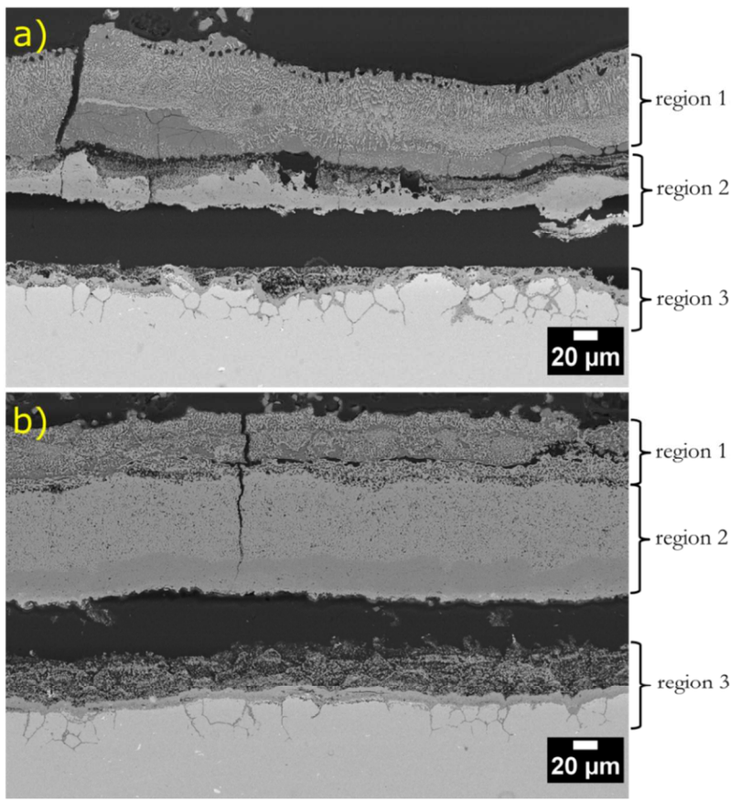

Figure 7. Morphology of corrosion products resulting from exposures involving thermal variations: (a) transition from 560 ^{o}C to 600 ^{o}C, experiment T7, and (b) transition from 600 ^{o}C to 560 ^{o}C, experiment T8.

Figure 8 reveals how thermal variation influences the degree of corrosion attack, by means of comparison of the mean thicknesses of the three regions of corrosion products, based on a minimum of 50 measurements. Compared with the pronounced increase in corrosion attack after 168 h of isothermal exposure at 600 ^{o}C, relative to 560 ^{o}C, thermal variation during corrosion exposure had a comparatively lower effect on the degree of attack. For the exposures that involved thermal variation, it is observed that an initially higher temperature of 600 ^{o}C (experiment T8), results in at least a 10 µm increase in average thickness of each of the corrosion product regions, compared with corrosion exposure that started with a lower temperature of 560 ^{o}C (experiment T7). Interestingly, considering the total exposure period of 168 h, Figure 8 also reveals that even with an initial or final exposure at

600 °C during thermal variation, the extent of corrosion attack is significantly higher than the corresponding isothermal exposure at 560 °C. On the basis of these observations, it is probable that a superheater will always suffer more corrosion attack once it encounters a temperature above its typical operating temperature. Furthermore, the sequence in which the material experiences a higher temperature during operation will influence the degree of corrosion attack such that an initial high temperature can propagate faster corrosion even during subsequent operation at lower temperatures.

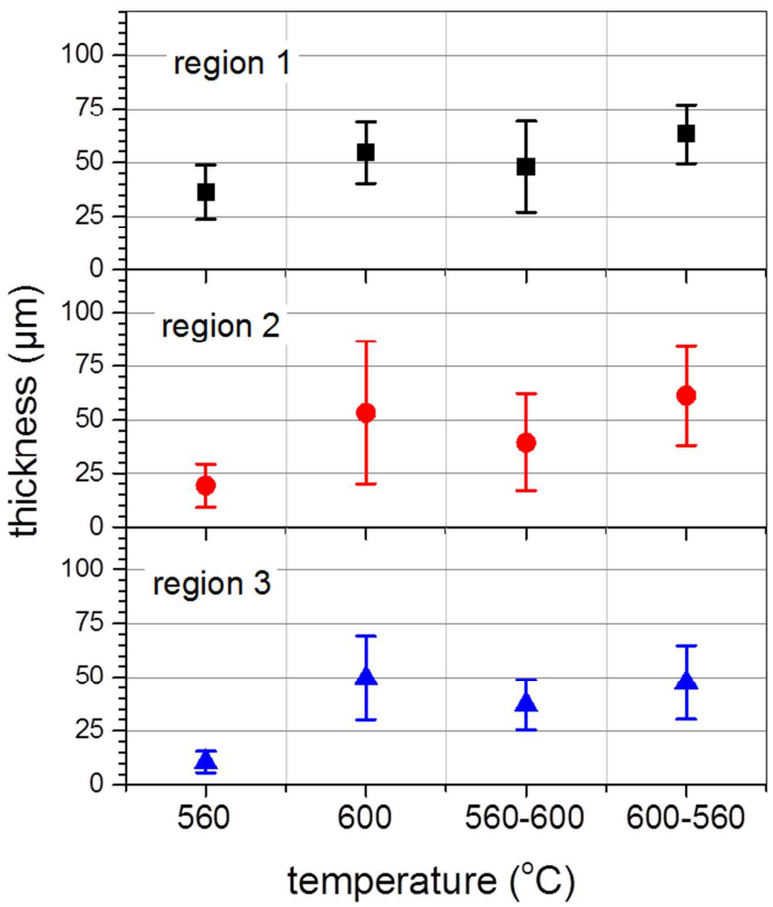

Figure 8. The mean thicknesses of the different regions of corrosion products after 168 h of exposure under isothermal (560 °C or 600 °C, experiments T2 and T6), and thermal variation (between 560 °C to 600 °C, experiments T7 and T8) conditions.

The observed influence of temperature on the extent of corrosion attack could relate to its effect on both the kinetics and thermodynamics of some principal processes involved in corrosion under biomass firing conditions. As stated in section 1.0, the breakdown of initially formed oxides due to their reaction with alkali chloride deposits, which is expected to be of relevance during the initiation stages of corrosion attack, can be influenced by temperature. Using as an example, the reaction between KCl and the Fe-Cr rich oxide that is known to form on austenitic stainless steels during the initial stages of corrosion [20,34] (reaction 2), thermodynamic calculations show that the Gibbs free energy change becomes less positive as temperature increases [35]. The fact that K_2CrO_4 was not observed in this study may not be due to the non-occurrence of this reaction to break down the initial chromia layer, but may be due to sulphation of the K_2CrO_4 as was observed in a previous study [36]. Similarly the Gibbs free energy change for reaction 2 becomes more negative with KCl vapour [35]. Thus, it is expected that increased generation of KCl vapour due to the temperature increase will enhance breakdown of the initially formed oxides on the sample surface, thereby providing access for transport of corrosive species. More so, based on literature, the sulphation of KCl which occurs under biomass firing conditions, can be enhanced when KCl is in the vapour phase [37]. Consequently, a higher partial pressure of HCl can be realized with temperature increase, as has been reported in reference [38] for the sulphation of condensed KCl. The Arrhenius plot of the sulphation rate reveals that the activation energy increases with respect to temperature between approximately 560 ºC and 600 ºC indicating a change in reaction mechanism [38,39]. Accordingly, it is likely that when temperature was increased in the present investigation, more chlorine was generated from dissociation of the resulting HCl [11,40], to sustain corrosion attack. Although the resulting HCl may leave the system via the flowing gas stream during the corrosion exposure, the observation of lesser corrosion attack on samples that were isothermally exposed at 560 ^{o}C, compared to samples that transitioned from 600 ^{o}C to 560 ^{o}C (Figure 8), strongly suggests that the enhanced generation of HCl at a higher temperature results in formation

of chlorine that incites more chlorination at the corrosion front. Based on the cyclic nature of the Cl-propagated corrosion mechanism [11,25,26], it is probable that part of the generated chlorine remained in the system to propagate corrosion during subsequent exposure at a lower temperature, thereby explaining the observed trend in thickness of corrosion products on samples isothermally exposed at 560 ^{o}C, compared to samples exposed under conditions that involved thermal variation (Figure 8). Such memory effect has been similarly observed in previous investigations with powders of Fe-Cr alloys, in which chlorine accumulation in the system sustained corrosion attack after removal of the chlorine source [41].

It is important to also note that within the temperature range investigated in the present study (560 ^{o}C-600 ^{o}C), Cr diffusion for oxide formation occurs mainly along the alloy grain boundaries [42]. In addition, the reaction of the major alloying elements (Fe, Cr, Ni) in the investigated alloy with chlorine is thermodynamically feasible within this temperature range [35], with the chlorination of Cr being particularly more favourable compared to Fe and Ni. Consequently, the expected promotion of Cr diffusion along the grain boundaries due to temperature increase will not lead to formation of a protective Cr_2O_3 under the investigated biomass firing conditions. Instead, preference for chlorination of Cr facilitates corrosion attack along grain boundaries as was observed in Figures 5 and 7.

One of the important factors controlling the nature of corrosion under chlorine-containing atmospheres is the stability of the metal chlorides resulting from the chlorination process. Increase in temperature provokes an increase in evaporation of metal chlorides, due to an increase in their vapour pressures [26]. Thus, with increasing temperatures, there is greater tendency for the metal chlorides formed at the corrosion front to evaporate, consequently leading to faster removal rates. Indeed, kinetic consideration of the high temperature reaction of metals under chlorinating atmospheres suggests an Arrhenius law controlled rate limiting step, which gives rise to exponential removal rates of the resulting reaction products upon temperature increase [43]. In line with the suggestion that the predominant transport of

species during corrosion under the investigated condition is probably via the gas phase, temperature provoked exponential removal rates are expected to also contribute to the observed influence of temperature on the degree of corrosion attack.

4. Conclusions

The influence of time and temperature on the KCl induced corrosion of austenitic stainless steel TP 347H FG under a gas mixture of 60 ppmv SO_2, 400 ppmv HCl, 6 vol% O_2, 12 vol% CO_2 , 3 vol% H_2O and N_2 (as balance), has been investigated. Corrosion of the alloy results in attack of Mn, Cr and Fe through a Cl-propagated mechanism.

Under isothermal conditions, corrosion attack increases with time. In particular, the thickness of the sulphate layer resulting from sulphation of KCl increases with time, suggesting that the reaction was incomplete even after 672 h. The thickness of the Fe-Cr-rich oxides concurrently increased with time suggesting that the sulphate layer on top of it does not effectively prevent transport of corrosive species.

Temperature increase from 560 ^{o}C to 600 ^{o}C significantly increases the degree of corrosion attack. Chlorination of alloying elements is enhanced at higher temperature due to increased vapour pressure of KCl and the corresponding enhanced sulphation to generate HCl. The vapour pressure of metal chlorides also increases with temperature leading to their faster removal from the corrosion front. Thus, operation of biomass fired power plants at high steam temperatures will result in increased corrosion attack on the superheaters. Temperature enhanced diffusion of Cr is not advantageous under biomass firing conditions because of the favourable chlorination of Cr. Increased preferential attack along grain boundaries therefore occurs when temperature is increased.

The order of temperatures during thermal variation influences the degree of corrosion attack such that initial exposure to a higher temperature will result in more corrosion attack probably because the high

partial pressure of chlorine generated at high temperatures sustains corrosion attack during subsequent exposure to a lower temperature. Thus, a single increase of the service temperature in real power plants as part of typical temperature fluctuations has a dramatic effect.

5. Acknowledgements

This work is part of the Danish Strategic Research Centre, Power Generation from Renewable Energy (GREEN). Funding from the Danish council for Strategic Research is acknowledged.

6. References

(1) Damoe, A. J.; Wu, H.; Frandsen, F. J.; Glarborg, P.; Sander, B. Impact of Coal Fly Ash Addition on Combustion Aerosols (PM 2.5) from Full-Scale Suspension-Firing of Pulverized Wood. *Energy & Fuels* **2014**, *28* (5), 3217–3223.

(2) The Danish Government https://stateofgreen.com/files/download/387.

(3) Montgomery, M.; Jensen, S. A.; Borg, U.; Biede, O.; Vilhelmsen, T. Experiences with High Temperature Corrosion at Straw-Firing Power Plants in Denmark. *Mater. Corros.* **2011**, *62* (7), 593–605.

(4) Frandsen, F. J. *Ash Formation, Deposition and Corrosion When Utilizing Straw for Heat and Power Production*; Dr. Techn. Thesis, Department of Chemical and Biochemical Engineering, Technical Univeristy of Denmark. ISBN: 9788792481405: Kongens Lyngby, 2011.

(5) Jensen, P. A.; Frandsen, F. J.; Hansen, J.; Dam-Johansen, K.; Henriksen, N.; Hörlyck, S. SEM Investigation of Superheater Deposits from Biomass-Fired Boilers. *Energy & Fuels* **2004**, *18* (2), 378–384.

(6) Michelsen, H. P.; Frandsen, F. J.; Dam-Johansen, K.; Larsen, O. H. Deposition and High Temperature Corrosion in a 10 MW Straw Fired Boiler. *Fuel Process. Technol.* **1998**, *54* (1-3), 95–108.

(7) Grabke, H. J.; Reese, E.; Spiegel, M. The Effects of Chlorides, Hydrogen Chloride, and Sulfur Dioxide in the Oxidation of Steels below Deposits. *Corros. Sci.* **1995**, *37* (7), 1023–1043.

(8) Montgomery, M.; Karlsson, A. In-Situ Corrosion Investigation at Masnedø CHP Plant - a Straw-Fired Power Plant. *Mater. Corros.* **1999**, *50* (10), 579–584.

(9) Antunes, R. A.; de Oliveira, M. C. L. Corrosion in Biomass Combustion: A Materials Selection Analysis and Its Interaction with Corrosion Mechanisms and Mitigation Strategies. *Corros. Sci.* **2013**, *76*, 6–26.

(10) Nielsen, H. P.; Frandsen, F. J.; Dam-Johansen, K.; Baxter, L. L. The Implications of Chlorine-Associated Corrosion on the Operation of Biomass-Fired Boilers. *Prog. Energy Combust. Sci.* **2000**, *26* (3), 283–298.

(11) Zahs, A.; Spiegel, M.; Grabke, H. The Influence of Alloying Elements on the Chlorine-Induced High Temperature Corrosion of Fe-Cr Alloys in Oxidizing Atmospheres. *Mater. Corros.* **1999**, *50* (10), 561–578.

(12) Li, Y. S.; Niu, Y.; Spiegel, M. High Temperature Interaction of Al/Si-Modified Fe–Cr Alloys with KCl. *Corros. Sci.* **2007**, *49* (4), 1799–1815.

(13) Nielsen, H. P.; Frandsen, F. J.; Dam-Johansen, K. Lab-Scale Investigations of High-Temperature Corrosion Phenomena in Straw-Fired Boilers. *Energy & Fuels* **1999**, *13* (6), 1114–1121.

(14) Karlsson, S.; Jonsson, T.; Hall, J.; Svensson, J.-E.; Liske, J. Mitigation of Fireside Corrosion of Stainless Steel in Power Plants: A Laboratory Study of the Influences of SO2 and KCl on Initial Stages of Corrosion. *Energy & Fuels* **2014**, *28* (5), 3102–3109.

(15) Lith, S. C. Van; Frandsen, F. J.; Montgomery, M.; Vilhelmsen, T.; Jensen, S. A. Lab-Scale Investigation of Deposit-Induced Chlorine Corrosion of Superheater Materials under Simulated Biomass-Firing Conditions. Part 1: Exposure at 560 °C. *Energy & Fuels* **2009**, *59* (10), 3457–3468.

(16) Okoro, S. C.; Montgomery, M.; Frandsen, F. J.; Pantleon, K. High Temperature Corrosion during Biomass Firing: Improved Understanding by Depth Resolved Characterisation of Corrosion Products. *Mater. High Temp.* **2015**, *32* (1-2), 92–101.

(17) Pettersson, J.; Folkeson, N.; Johansson, L.-G.; Svensson, J.-E. The Effects of KCl, K2SO4 and K2CO3 on the High Temperature Corrosion of a 304-Type Austenitic Stainless Steel. *Oxid. Met.* **2011**, *76* (1-2), 93–109.

(18) Henderson, P.; Szakálos, P.; Pettersson, R.; Andersson, C.; Högberg, J. Reducing Superheater Corrosion in Wood-Fired Boilers. *Mater. Corros.* **2006**, *57* (2), 128–134.

(19) Aho, M.; Vainikka, P.; Taipale, R.; Yrjas, P. Effective New Chemicals to Prevent Corrosion due to Chlorine in Power Plant Superheaters. *Fuel* **2008**, *87* (6), 647–654.

(20) Pettersson, J.; Svensson, J.-E.; Johansson, L.-G. KCl-Induced Corrosion of a 304-Type Austenitic Stainless Steel in O2 and in O2 + H2O Environment: The Influence of Temperature. *Oxid. Met.* **2009**, *72* (3-4), 159–177.

(21) Okoro, S. C.; Kiamehr, S.; Montgomery, M.; Frandsen, F. J.; Pantleon, K. Effect of Flue Gas Composition on Deposit Induced High Temperature Corrosion under Laboratory Conditions Mimicking Biomass Firing. Part I: Exposures in Oxidizing and Chlorinating Atmospheres. *Mater. Corros.* **2017**, *68* (5), 499–514.

(22) Karlsson, S.; Larsson, E.; Jonsson, T.; Svensson, J.-E.; Liske, J. A Laboratory Study of the in Situ Sulfation of Alkali Chloride Rich Deposits: Corrosion Perspective. *Energy & Fuels* **2016**, *30* (9), 7256–7267.

(23) Hansson, A. N.; Danielsen, H.; Grumsen, F. B.; Montgomery, M. Microstructural Investigation of the Oxide Formed on TP 347H FG during Long-Term Steam Oxidation. *Mater. Corros.* **2009**, *61* (8), 665–675.

(24) Kiamehr, S.; Dahl, K. V.; Montgomery, M.; Somers, M. A. J. KCl-Induced High Temperature

Corrosion of Selected Commercial Alloys. Part I: Chromia-Formers. *Mater. Corros.* **2015**, *66* (12), 1414–1429.

(25) Okoro, S. C.; Montgomery, M.; Frandsen, F. J.; Pantleon, K. Effect of Water Vapor on High-Temperature Corrosion under Conditions Mimicking Biomass Firing. *Energy & Fuels* **2015**, *29* (9), 5802–5815.

(26) Zahs, A.; Spiegel, M.; Grabke, H. J. Chloridation and Oxidation of Iron, Chromium, Nickel and Their Alloys in Chloridizing and Oxidizing Atmospheres at 400–700°C. *Corros. Sci.* **2000**, *42* (6), 1093–1122.

(27) Li, Y. S.; Spiegel, M. Models Describing the Degradation of FeAl and NiAl Alloys Induced by ZnCl2–KCl Melt at 400–450 °C. *Corros. Sci.* **2004**, *46* (8), 2009–2023.

(28) Yamada, K.; Tomono, Y.; Morimoto, J.; Sasaki, Y.; Ohmori, A. Hot Corrosion Behavior of Boiler Tube Materials in Refuse Incineration Environment. *Vacuum* **2002**, *65* (3-4), 533–540.

(29) Bender, R.; Schütze, M. The Role of Alloying Elements in Commercial Alloys for Corrosion Resistance in Oxidizing-Chloridizing Atmospheres Part I: Literature Evaluation and Thermodynamic Calculations on Phase Stabilities. *Mater. Corros.* **2003**, *54* (8), 567–586.

(30) Okoro, S. C.; Kiamehr, S.; Montgomery, M.; Frandsen, F. J.; Pantleon, K. Effect of Flue Gas Composition on Deposit Induced High Temperature Corrosion under Laboratory Conditions Mimicking Biomass Firing. Part II: Exposures in SO 2 Containing Atmospheres. *Mater. Corros.* **2017**, *68* (5), 515–528.

(31) Paneru, M.; Stein-Brzozowska, G.; Maier, J.; Scheffknecht, G. Corrosion Mechanism of Alloy 310 Austenitic Steel beneath NaCl Deposit under Varying SO2 Concentrations in an Oxy-Fuel Combustion Atmosphere. *Energy & Fuels* **2013**, *27* (10), 5699–5705.

(32) Chevalier, S. Mechanisms and Kinetics of Oxidation. In *Shreir's Corrosion*; Cottis, B., Graham, M., Lindsay, R., Lyon, S., Richardson, T., Scantlebury, D., Stott, H., Eds.; Elsevier, 2010; pp

132–152.

(33) Hay, K. A.; Hicks, F. G.; Holmes, D. R. The Transport Properties and Defect Structure of the Oxide (Fe, Cr)2O3 Formed on Fe-Cr Alloys. *Mater. Corros. und Korrosion* **1970**, *21* (11), 917–924.

(34) Asteman, H.; Svensson, J.-E.; Johansson, L.-G.; Norell, M. Indication of Chromium Oxide Hydroxide Evaporation During Oxidation of 304L at 873 K in the Presence of 10% Water Vapor. *Oxid. Met.* **1999**, *52* (1/2), 95–111.

(35) Bale, C. W.; Bélisle, E.; Chartrand, P.; Decterov, S. A.; Eriksson, G.; Hack, K.; Jung, I.-H.; Kang, Y.-B.; Melançon, J.; Pelton, A. D.; et al. FactSage Thermochemical Software and Databases — Recent Developments. *Calphad* **2009**, *33* (2), 295–311.

(36) Okoro, S. C.; Montgomery, M.; Frandsen, F. J.; Pantleon, K. High Temperature Corrosion under Laboratory Conditions Simulating Biomass-Firing: A Comprehensive Characterization of Corrosion Products. *Energy & Fuels* **2014**, *28* (10), 6447–6458.

(37) Iisa, K.; Lu, Y.; Salmenoja, K. Sulfation of Potassium Chloride at Combustion Conditions. *Energy & Fuels* **1999**, *13* (6), 1184–1190.

(38) Sengeløv, L. W.; Hansen, T. B.; Bartolome, C.; Wu, H.; Pedersen, K. H.; Frandsen, F. J.; Jensen, A. D.; Glarborg, P. Sulfation of Condensed Potassium Chloride by SO2. *Energy & Fuels* **2013**, *27*, 3283–3289.

(39) Hu, Z.; Wang, X.; Wang, Z.; Wang, Y.; Tan, H. Segmented Kinetic Investigation on Condensed KCl Sulfation in SO2 /O2 /H2O at 523–1023 K. *Energy & Fuels* **2014**, *28* (12), 7560–7568.

(40) Over, H.; Schomäcker, R. What Makes a Good Catalyst for the Deacon Process? *ACS Catal.* **2013**, *3* (5), 1034–1046.

(41) Salmenoja, K.; Hupa, M.; Backman, R. Laboratory Studies on the Influence of Gaseous HCl on Fireside Corrosion of Superheaters. *J. Inst. Energy* **1999**, *72*, 127–133.

(42) Hansson, A. N.; Hattel, J. H.; Dahl, K. V; Somers, M. A. J. Modelling Cr Depletion under a Growing Cr2O3 Layer on Austenitic Stainless Steel: The Influence of Grain Boundary Diffusion. *Model. Simul. Mater. Sci. Eng.* **2009**, *17* (3), 19.

(43) Rammer, B.; Galetz, M. C. Kinetics of Volatilization of High Temperature Corrosion Products and Its Application to Chlorine Corrosion. *Mater. Corros.* **2017**, *68* (2), 186–196.

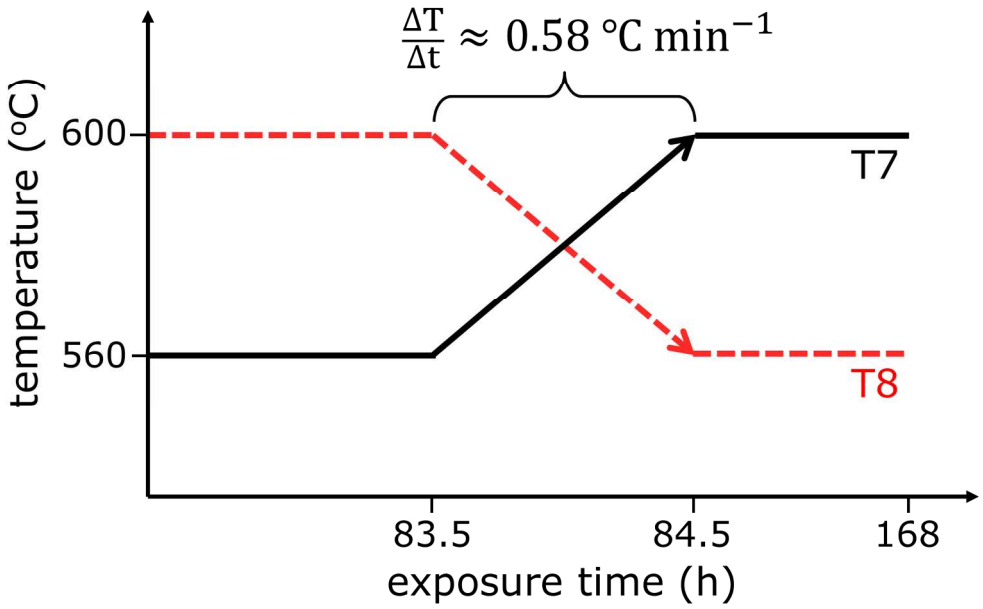

Figure 1. Schematic illustration of the thermal variation sequence in experiments T7 and T8.

182x117mm (300 x 300 DPI)

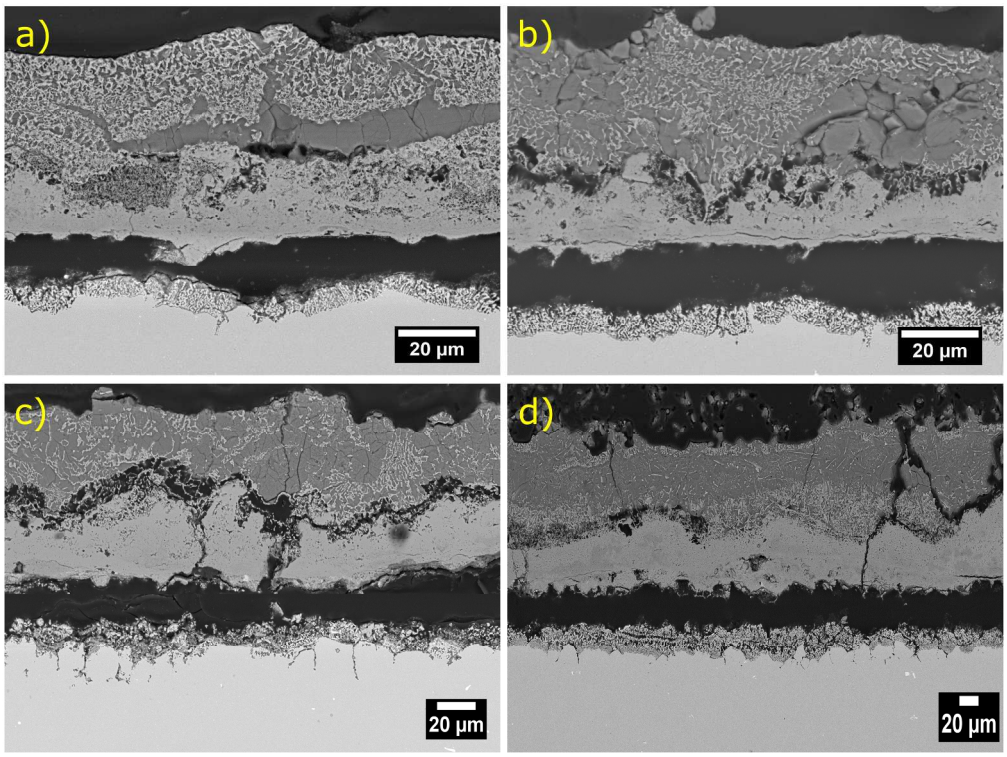

Figure 2. Morphology of corrosion products after isothermal exposure at 560 oC for different durations. (a) 83.3 h, experiment T1, (b) 168 h, experiment T2, (c) 336 h, experiment T3, and (d) 672 h, experiment T4. The schematic in (e) provides a representation of the typical regions of corrosion products.

242x181mm (300 x 300 DPI)

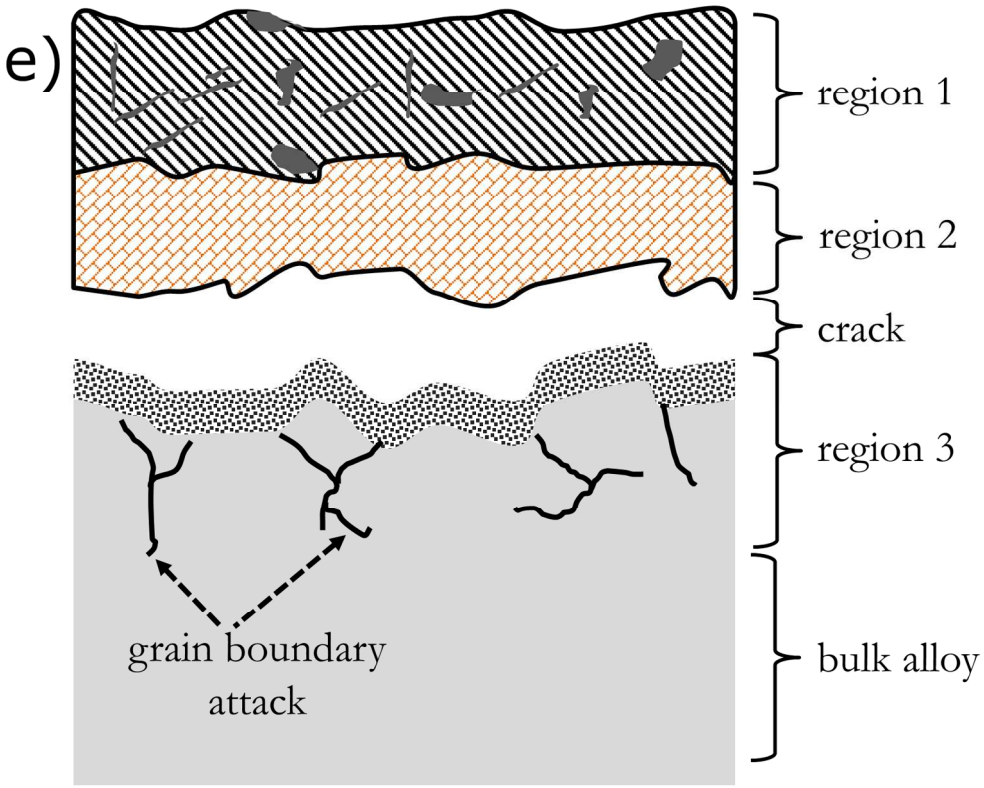

Figure 2. Morphology of corrosion products after isothermal exposure at 560 oC for different durations. (a) 83.3 h, experiment T1, (b) 168 h, experiment T2, (c) 336 h, experiment T3, and (d) 672 h, experiment T4. The schematic in (e) provides a representation of the typical regions of corrosion products.

145x120mm (300 x 300 DPI)

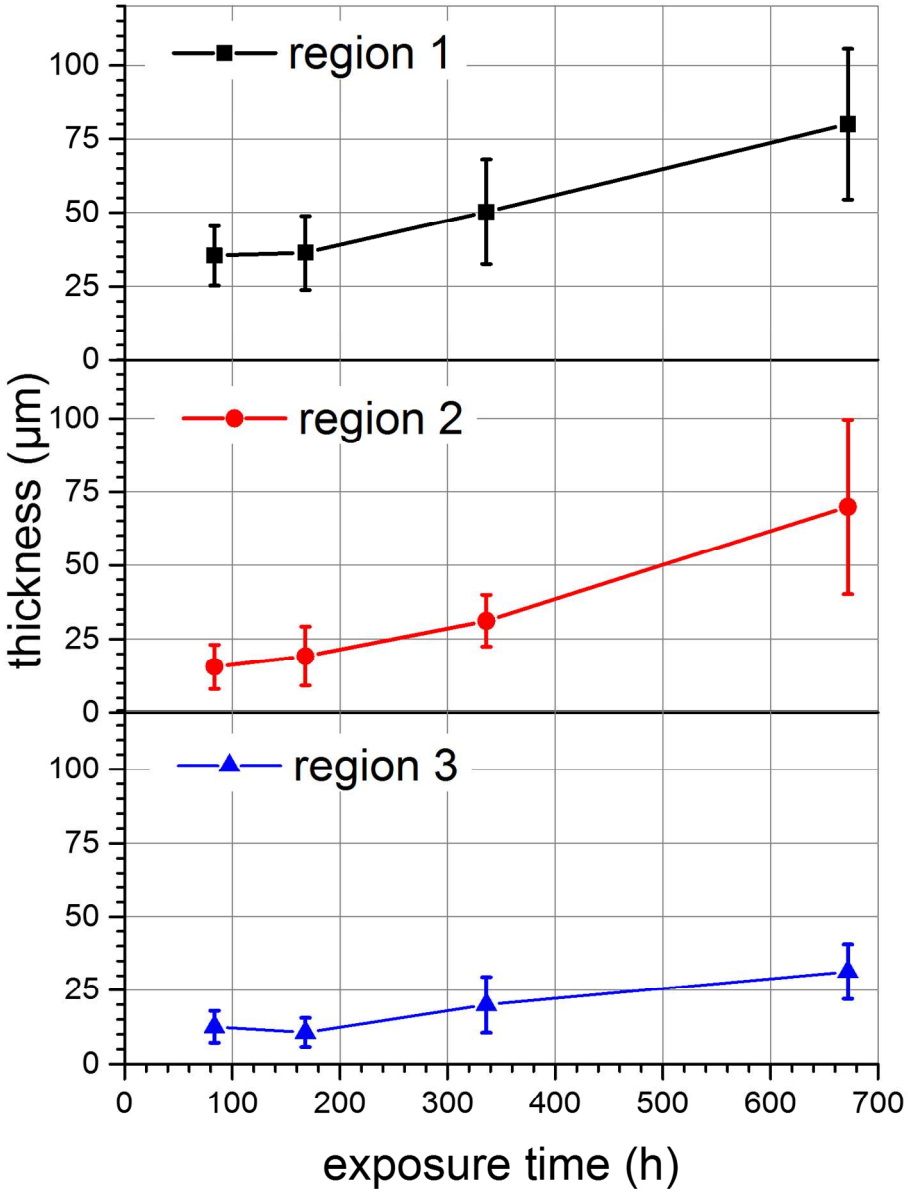

Figure 3. The mean thicknesses of the different regions of corrosion products as a function of exposure time at 560 oC (experiments T1-T4). The error bars outline the corresponding standard deviation.

139x179mm (300 x 300 DPI)

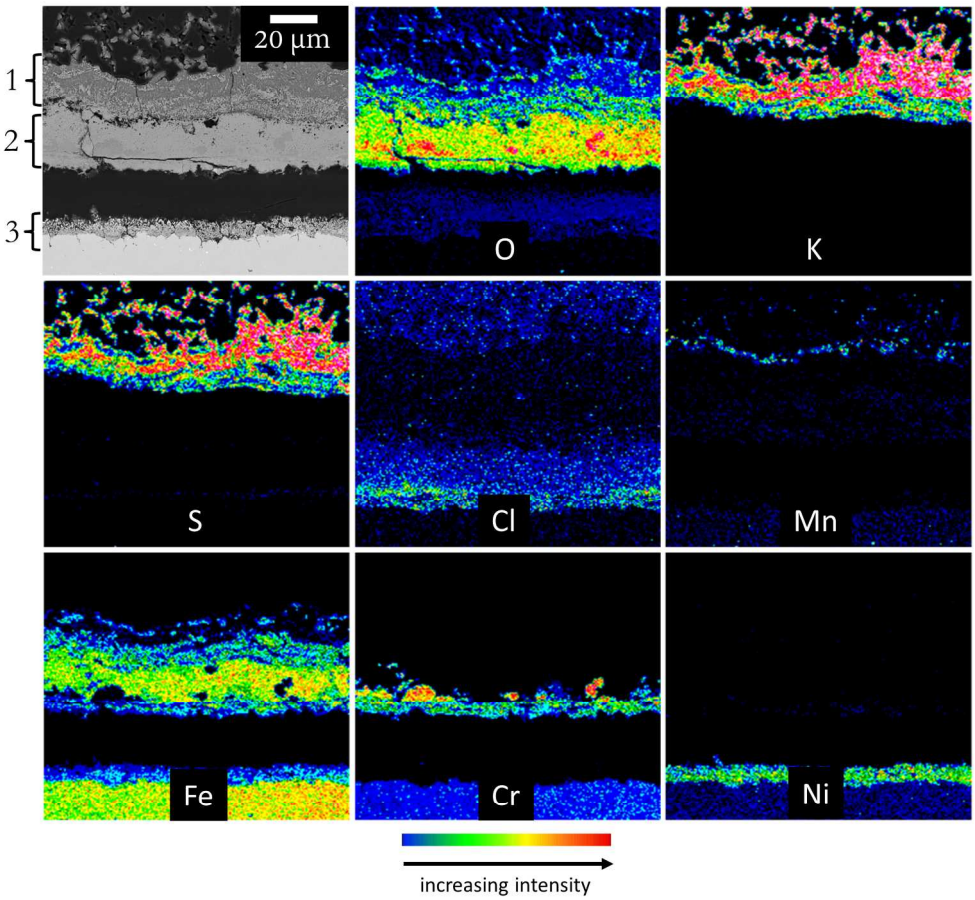

Figure 4. EDS maps showing the chemical composition of the different regions of corrosion products after 672 h of isothermal exposure at 560 oC.

194x176mm (300 x 300 DPI)

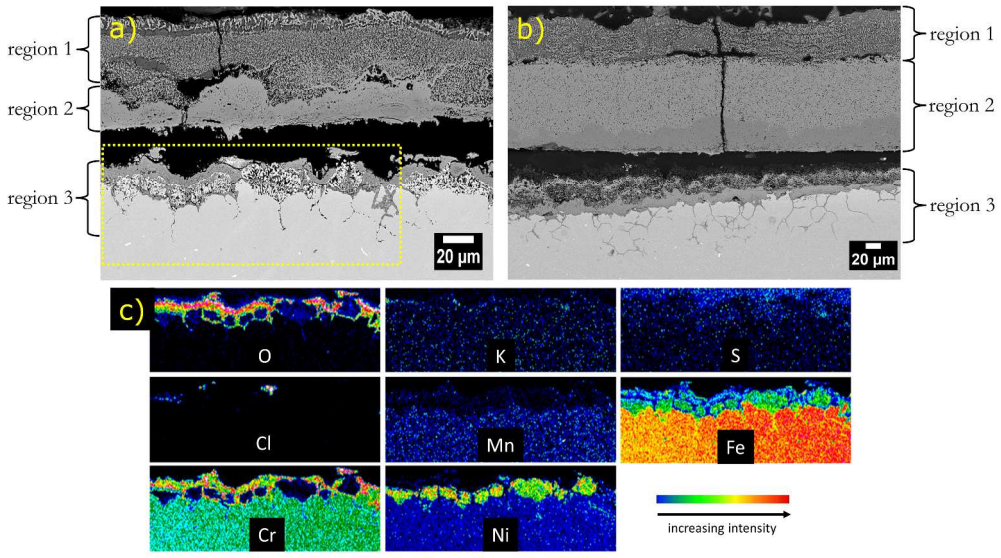

Figure 5. Morphology of corrosion products after isothermal exposures at 600 oC for (a) 83.5 h, experiment T5 and (b) 168 h, experiment T6. (c) EDS maps of the selected area in (a).

305x172mm (300 x 300 DPI)

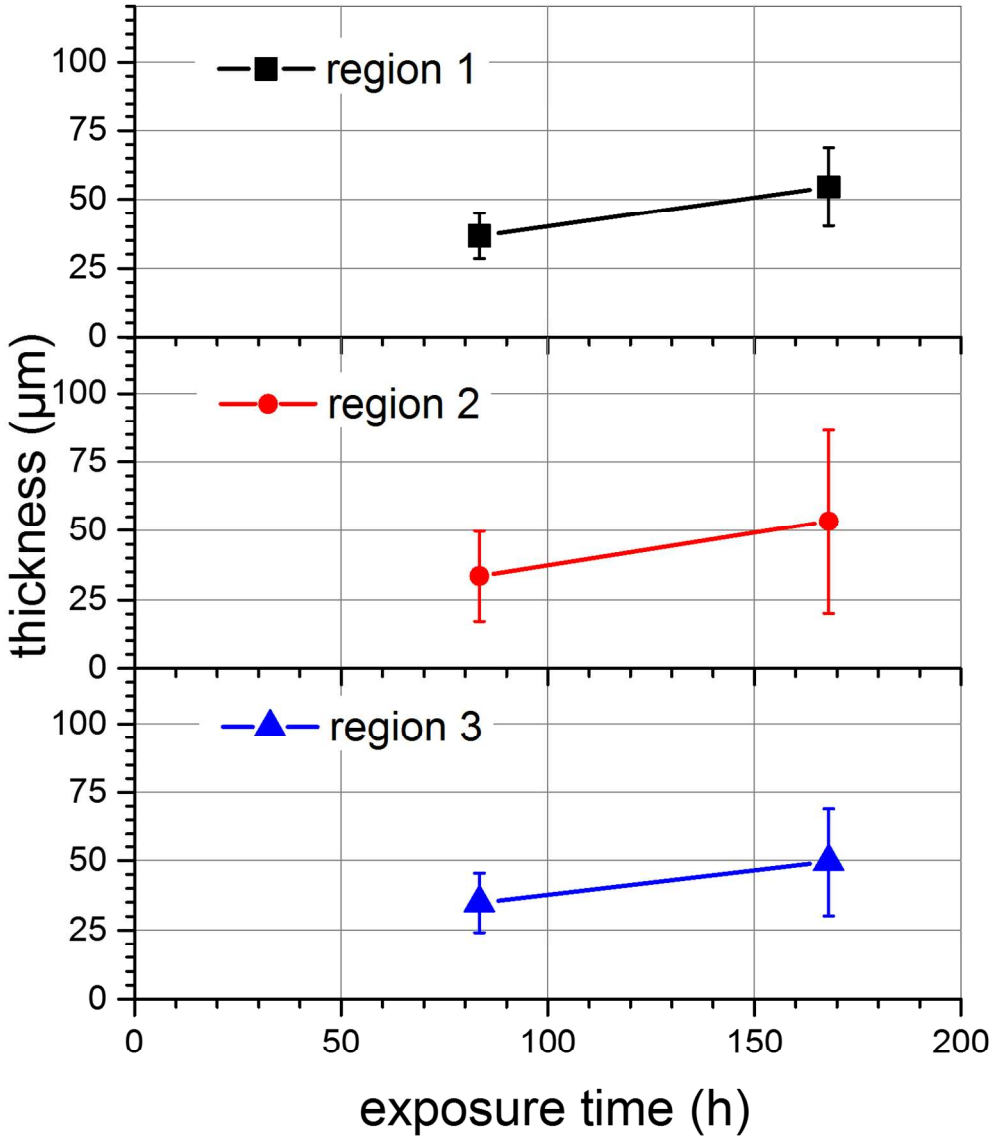

Figure 6. The mean thicknesses of the different regions of corrosion products after isothermal exposure at 600 oC for different times (experiments T5 and T6). The error bars outline the corresponding standard deviation.

136x156mm (300 x 300 DPI)

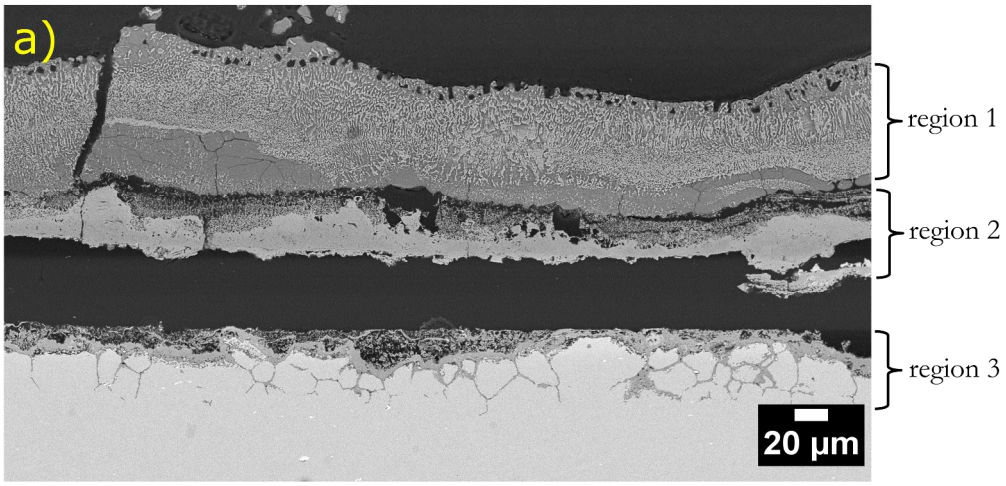

Figure 7. Morphology of corrosion products resulting from exposures involving thermal variations: (a) transition from 560 oC to 600 oC, experiment T7, and (b) transition from 600 oC to 560 oC, experiment T8.

293x141mm (300 x 300 DPI)

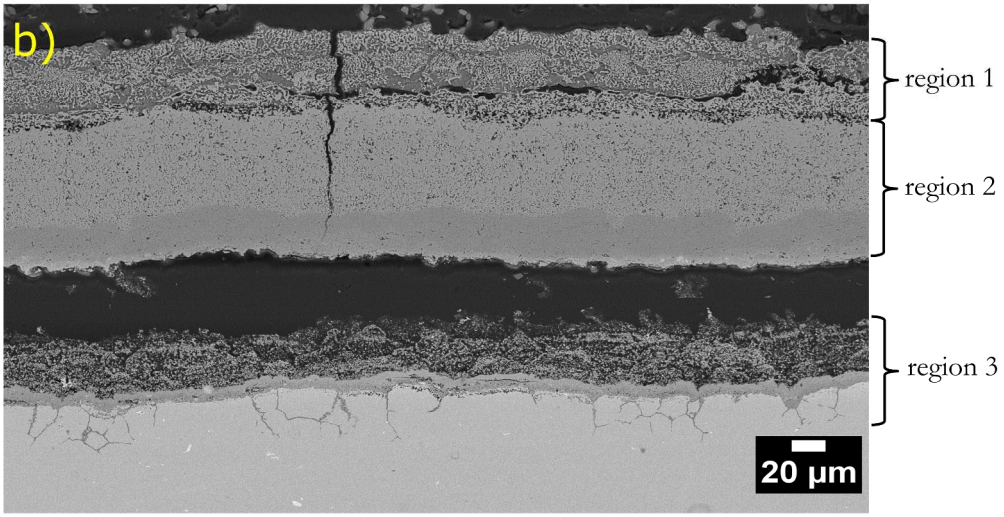

Figure 7. Morphology of corrosion products resulting from exposures involving thermal variations: (a) transition from 560 oC to 600 oC, experiment T7, and (b) transition from 600 oC to 560 oC, experiment T8.

294x151mm (300 x 300 DPI)

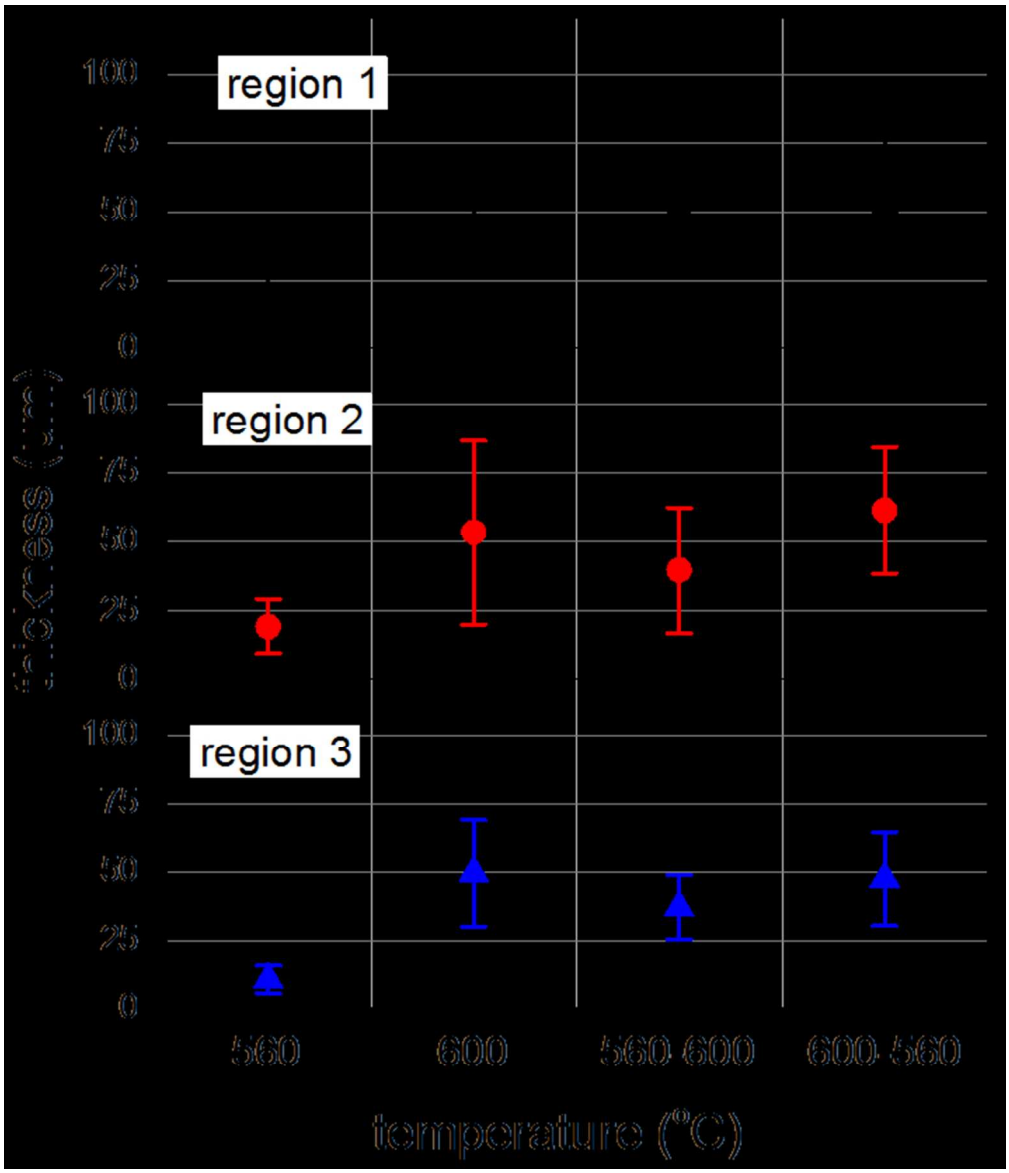

Figure 8. The mean thicknesses of the different regions of corrosion products after 168 h of exposure under isothermal (560 oC or 600 oC, experiments T2 and T6), and thermal variation (between 560 oC to 600 oC, experiments T7 and T8) conditions.

120x140mm (150 x 150 DPI)